

## The strength and rheology of methane clathrate hydrate

William B. Durham

Lawrence Livermore National Laboratory, University of California, Livermore, California, USA

Stephen H. Kirby and Laura A. Stern

U.S. Geological Survey, Menlo Park, California, USA

Wu Zhang<sup>1</sup>

Lawrence Livermore National Laboratory, University of California, Livermore, California, USA

Received 12 March 2002; revised 12 September 2002; accepted 28 October 2002; published 2 April 2003.

[1] Methane clathrate hydrate (structure I) is found to be very strong, based on laboratory triaxial deformation experiments we have carried out on samples of synthetic, high-purity, polycrystalline material. Samples were deformed in compressional creep tests (i.e., constant applied stress,  $\sigma$ ), at conditions of confining pressure  $P = 50$  and  $100$  MPa, strain rate  $4.5 \times 10^{-8} \leq \dot{\epsilon} \leq 4.3 \times 10^{-4} \text{ s}^{-1}$ , temperature  $260 \leq T \leq 287$  K, and internal methane pressure  $10 \leq P_{\text{CH}_4} \leq 15$  MPa. At steady state, typically reached in a few percent strain, methane hydrate exhibited strength that was far higher than expected on the basis of published work. In terms of the standard high-temperature creep law,  $\dot{\epsilon} = A\sigma^n e^{-(E^*+PV^*)/RT}$  the rheology is described by the constants  $A = 10^{8.55} \text{ MPa}^{-n} \text{ s}^{-1}$ ,  $n = 2.2$ ,  $E^* = 90,000 \text{ J mol}^{-1}$ , and  $V^* = 19 \text{ cm}^3 \text{ mol}^{-1}$ . For comparison, at temperatures just below the ice point, methane hydrate at a given strain rate is over 20 times stronger than ice, and the contrast increases at lower temperatures. The possible occurrence of syntectonic dissociation of methane hydrate to methane plus free water in these experiments suggests that the high strength measured here may be only a lower bound. On Earth, high strength in hydrate-bearing formations implies higher energy release upon decomposition and subsequent failure. In the outer solar system, if Titan has a 100-km-thick near-surface layer of high-strength, low-thermal conductivity methane hydrate as has been suggested, its interior is likely to be considerably warmer than previously expected. **INDEX TERMS:** 3902 Mineral Physics: Creep and deformation; 4540 Oceanography: Physical: Ice mechanics and air/sea/ice exchange processes; 5104 Physical Properties of Rocks: Fracture and flow; 6280 Planetology: Solar System Objects: Saturnian satellites; **KEYWORDS:** Gas hydrates, creep of ice, planetary ices, mechanical stability, Titan, Mars

**Citation:** Durham, W. B., S. H. Kirby, L. A. Stern, and W. Zhang, The strength and rheology of methane clathrate hydrate, *J. Geophys. Res.*, 108(B4), 2182, doi:10.1029/2002JB001872, 2003.

### 1. Introduction

[2] Hydrocarbon clathrate hydrates are important intermolecular compounds and naturally occurring minerals that occur on submarine continental margins and regions of arctic permafrost [Kvenvolden, 1993, 2000; Sloan, 1998]. They are also expected to occur within medium-to-large-sized icy moons of the outer solar system [Loveday et al., 2001; Lunine and Stevenson, 1985], and in the polar regions of Mars [Jakosky et al., 1995; Miller and Smythe, 1970]. On Earth, their global abundance and distribution suggest that they may become energy resources of the future [Collett, 2000; Kvenvolden, 1993]. The response of gas hydrate formations to tectonic, gravitational, and anthropogenic forces is a function of the mechanical strength and geometric distribution of the phases present (sediment, gas

hydrate, water) and the cohesion and frictional resistance between grains. Concentrations of distributed gas hydrate in formations identified as hydrate bearing are poorly known because of the difficulty in making direct observations; recent estimates put the hydrate concentration as low as 1–2 vol.% in marine sediments [Holbrook et al., 1996] and as high as several tens of percent in permafrost regions [Dallimore and Collett, 1999]. In deposits where hydrate is located structurally between sediment grains [Helgerud, 2001] or as cementation around contacting grains [Guerin et al., 1999], grain-to-grain cohesion and frictional resistance, from which “soft” sediments derive their strength [Martinson, 1994; Mulder and Alexander, 2000], can be affected, implying an effect on formation strength even at low concentrations of intergranular hydrate. At higher concentrations, we can expect a formation-strengthening effect from a solid phase in pores by analogy to strength enhancement in frozen soils at volume concentrations above 20–30% [Andersland and Ladanyi, 1994] and from general theory and experience with rheologies of mixtures [Handy, 1994; Tullis et al., 1991].

<sup>1</sup>Now at West Virginia University, Morgantown, West Virginia, USA.

[3] Previous measurements of the yield strength of methane hydrate [Stern *et al.*, 1996] and of gas hydrate-bearing sediment [Cameron *et al.*, 1990; Parameswaran *et al.*, 1989] indicated that the strength of those test materials was roughly comparable to that of ice. The response of test specimens in those studies may have been influenced by impurities of residual solid or liquid H<sub>2</sub>O, or by a lack of sufficient confining pressure to suppress fracture. For example, Stern *et al.* [1996] reported that X-ray diffraction measurements of their sample material before and after deformation showed that up to 25 vol.% of water ice developed within samples during compaction and deformation testing, despite the maintenance of high confining pressures and low temperatures. There have been other indications that methane hydrate is stronger than water ice. A preliminary experiment to this study by Zhang *et al.* [1999] produced an astonishing morphology that reflected the manifest strength contrast between water ice and methane hydrate (Figure 1). More recently, Winters *et al.* [2001] showed that during the initial transient stage of deformation, Ottawa sand with methane hydrate as pore filling is significantly stronger than the same sand with ice as pore filling. Helgerud [2001] also recently showed that at  $-20^{\circ}\text{C}$ , full compaction of granular methane hydrate requires more than ten times the stress as that required to compact granulated ice.

[4] Until recently, evaluating the effects of hydrocarbon hydrates on sediment properties was difficult because many fundamental physical properties had not been directly measured on pure structure I (sI) methane hydrate CH<sub>4</sub>·5.75H<sub>2</sub>O [Sloan, 1998], thought to be the principal hydrocarbon hydrate in nature [Kvenvolden, 1993]. Although plentiful, gas hydrates on Earth occur only in remote locations and are usually mixed with soil in arctic permafrost or with marine sediments. Pure and unaltered samples of naturally occurring gas hydrates have therefore been difficult to recover, and their properties remain poorly known. This situation has been partially alleviated by the development of a method for synthesizing pure methane hydrate with highly reproducible physical and chemical characteristics, in sufficient volume to allow measurements of properties [Stern *et al.*, 1996, 1998, 2000]. The objective of the present study is to characterize the rheological properties of methane hydrate at terrestrial conditions. While natural gas hydrates occur most often as a pore-filling phase in ocean sediments rather than in bulk, the first step toward characterizing the mechanical competence of hydrate formations is to understand the physics of deformation of the pure material.

## 2. Apparatus and Techniques

[5] We deform samples in the standard mode of rock mechanics, called conventional triaxial testing, in which a cylindrical sample is confined on the outside by gas at pressure  $P$  that is sufficiently high to suppress fracturing and microfracturing, thus keeping the deformation strictly in the ductile field and assuring that the rheology measured is an intrinsic material property. Samples are deformed in compression by the application of an axial stress  $\sigma$ , called the differential stress, which is sufficiently high to cause the sample to yield and permanently shorten at a strain rate  $\dot{\epsilon}$  defined as the increment of length change per unit length per increment of time. Sample volume remains constant, so



**Figure 1.** Posttest appearance of a composite sample of water ice (top) and methane hydrate (bottom), illustrating the strength contrast between the two phases. Sample was from a series of tests made previously to the current study. The extreme heterogeneity in composition occurred because the top end of the sample was inadvertently warmed during sample preparation, causing the upper portion to decompose to ice plus methane gas. The sample was compressed axially with a differential stress of 3.5 MPa at 260 K. The ice portion shortened at a rate of roughly  $1 \times 10^{-4} \text{s}^{-1}$  while the methane hydrate shortened at a rate that was about 4.5 orders of magnitude slower.

that as the sample undergoes permanent shortening, it also expands radially.

[6] The steady state rheology of most crystalline materials can be described by a mechanical equation of state or constitutive relationship [Poirier, 1985] of the form:

$$\dot{\epsilon} = A\sigma^n e^{(-E^* + PV^*)/RT}, \quad (1)$$

where  $R$  is the gas constant and  $A$ ,  $n$ ,  $E^*$ , and  $V^*$  are material-specific flow parameters, called the preexponential constant, the stress exponent, the activation energy, and the activation

volume, respectively. Our objective is to characterize the rheology of methane hydrate, i.e., to identify the parameters in equation (1). Steady state means that  $\dot{\epsilon}$  does not change in an increment of strain if  $\sigma$ ,  $T$ , and  $P$  do not change. Steady state cannot be assumed, but must be confirmed by experiment. On the basis of experience with ice and other oxides in high-temperature creep of fully dense, monomineralic materials, we anticipate that steady state deformation is reached at strains of a few percent after the first application of, or change in,  $\sigma$ .

[7] The experiments described here are creep tests, wherein  $\sigma$  is held constant and  $\dot{\epsilon}$  is the dependent variable. Most of the samples were tested under multiple sets of conditions, that is,  $\sigma$ ,  $T$ , or  $P$  were stepped to new values after steady state, or at least the appearance of steady state, was achieved in the previous step.

[8] High-purity samples of polycrystalline methane hydrate were synthesized by statically reacting granular seed ice and pressurized methane gas in cylindrical molds with an inner diameter of 25 mm [Stern *et al.*, 1996, 1998, 2000]. The approximately 0.2 mm grain-size seed ice was prepared by crushing and sieving bubble-free ice that was grown from triple-distilled water. Observation of the resulting hydrate by scanning electron microscopy (SEM) shows that the final material consists of 0.25-mm-diameter clusters of dense, smaller grains, typically 20–40  $\mu\text{m}$ , shown in Figure 2. As synthesized, the resulting hydrate has a porosity of about 29% and a hydrate number of  $5.89 \pm 0.1$  [Stern *et al.*, 2000]. For deformation, samples were cut to a length of about 63 mm and sealed in tight-fitting tubes of indium metal (0.5-mm-wall thickness) between hard steel end caps (Figure 3). One sample (number 459) was prepared by disaggregating and pulverizing pieces of synthesized hydrate with mortar and pestle, then packing the powder with the impacts of light hammer blows directly into the indium tube. Sample cutting and jacketing was done by hand in a vented glove box at temperatures that varied from 77 to roughly 120 K. Once sealed, the samples were stored at 77 K until testing.

[9] The upper end cap of the sample (Figures 3c and 3d) is the termination of a single piece of steel that serves several functions. It is the static base against which the sample is compressed by a piston moving upward through the lower seal of the pressure vessel; it is the containment for the top seal of the pressure vessel; and it is the sample force gage. The elastic strain of the gage length (Figures 3c and 3d) is directly proportional to  $\sigma$ , hence it is truly an “internal” force gage, although the elastic strain of the gage is measured by a transducer sitting outside the pressurized volume. Joined to a through hole in the upper end cap is a length of small-diameter, high-pressure tubing, which allows chemical communication to the sample (Figure 3d). For the experiments described here, we used this conduit to control the methane pressure,  $P_{\text{CH}_4}$ , in the sample. To ensure that sample material did not intrude into this pore pressure line and that  $P_{\text{CH}_4}$  was communicated evenly across the top of the sample, we placed a porous metal disc directly between the sample and end cap (Figure 3d).

[10] We have found that no matter how careful the sample handling, the absence of free water cannot be guaranteed. We have therefore adopted a strategy of melting any contaminant water phase and squeezing it from the sample

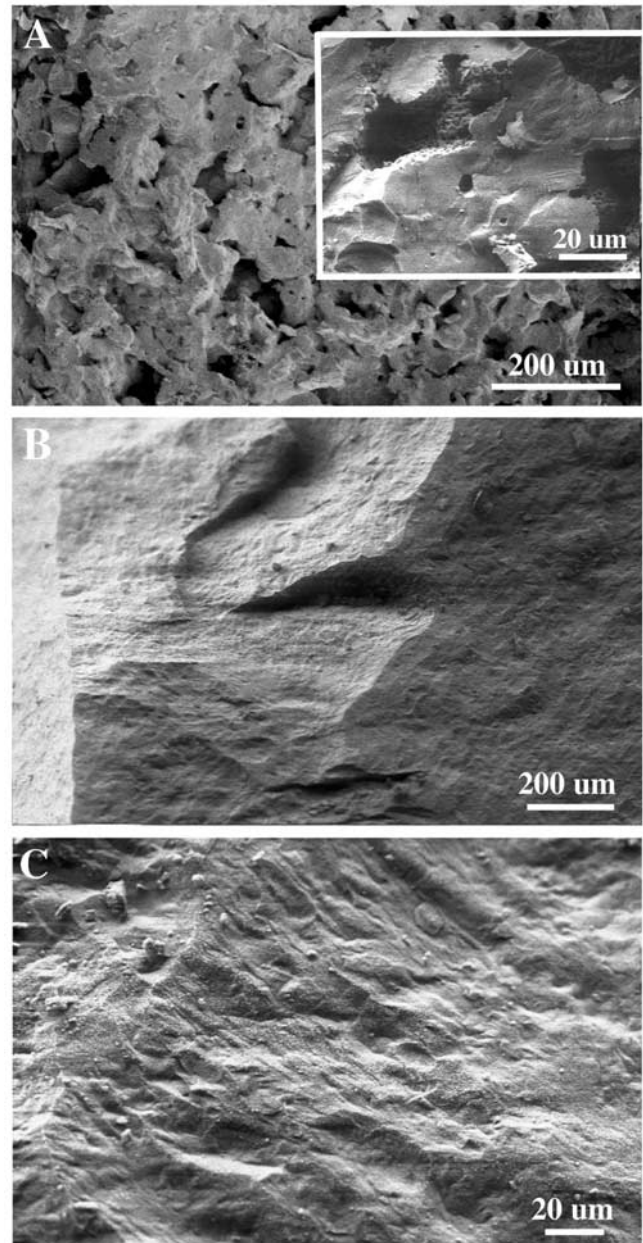


**Figure 2.** Scanning electron microscope (SEM) images of fracture surfaces through methane hydrate starting material (a and b) and after hydrostatic compaction and deformation (c; sample 459). Although the relict texture of the granular ice reactant is apparent in Figure 2a, the hydrate product is found to be densely recrystallized to 20–40  $\mu\text{m}$  grains surrounding open pores (Figure 2b). Samples after testing (Figure 2c) are fully dense, with no obvious evidence of residual porosity or of an ice contaminant phase. Samples for SEM observation were prepared and imaged under vacuum at temperatures below  $-160^\circ\text{C}$ , at 1–2 kV.

before beginning the first deformation step. Porosity is also eliminated prior to the start of deformation, and the creation of new porosity is suppressed throughout the experiment. We achieved these conditions by the following procedure:

1. Transfer the sample assembly as quickly as possible from storage at 77 K to the pressure vessel at about

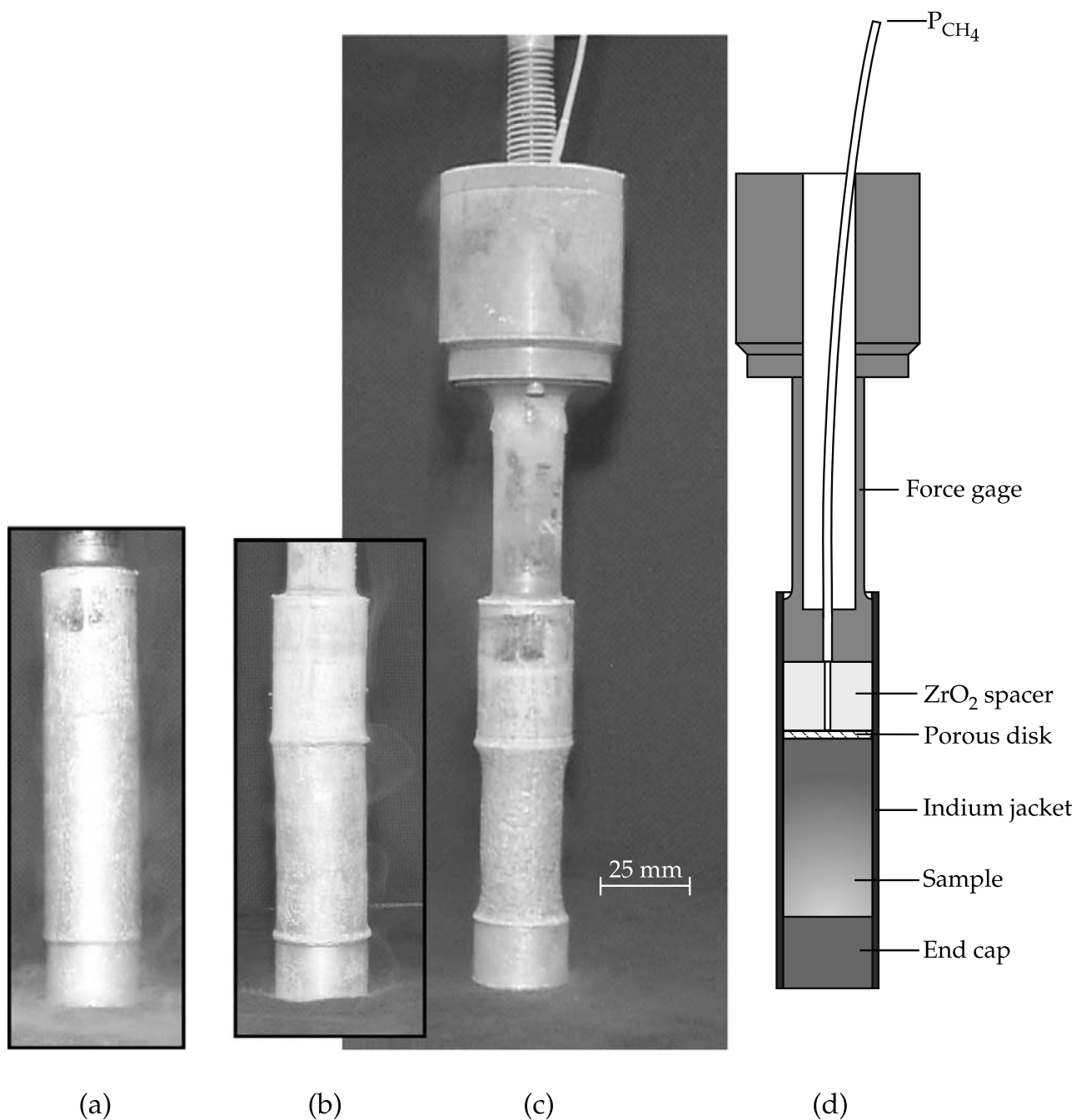


**Figure 3.** Photographs of three samples (a) before compaction under hydrostatic pressure, sample 461, and (b and c) after hydrostatic pressurization to 100 MPa at 280 K, samples 459 and 457, respectively, and (d) cross-sectional sketch of the assembly. Photographs and sketch are at approximately the same scale. End cap, polycrystalline methane hydrate sample, porous disc,  $ZrO_2$  spacer, and narrow neck of the force gage are surrounded by a 0.5-mm-indium tube that is sealed to metal column parts at its very top and bottom. High gas pressure outside the jacket squeezes all porosity out of the sample, which begins with a length of about 63 mm (Figure 3a), but shortens and narrows under confining pressure. The volume collapse from Figure 3a to Figure 3b is typical (about 30%); the much greater volume collapse of 457 in Figure 3c is anomalous. Figure 3c shows the entire column assembly of sample plus force gage. The narrow, thin-walled portion of the force gage (see Figure 3d) is the gage length, whose elastic distortion is a direct measure of the axial force on the sample. The wide portion at the top is the pressure vessel plug. Note that the main pressure seal is made at the stepped portion of the plug, so that the force measured by the gage is not affected by tractions at the pressure seal. The narrow tube emerging from the top of the plug is the pore pressure line, which reaches the porous disc and sample through an axial hole in the  $ZrO_2$  spacer.

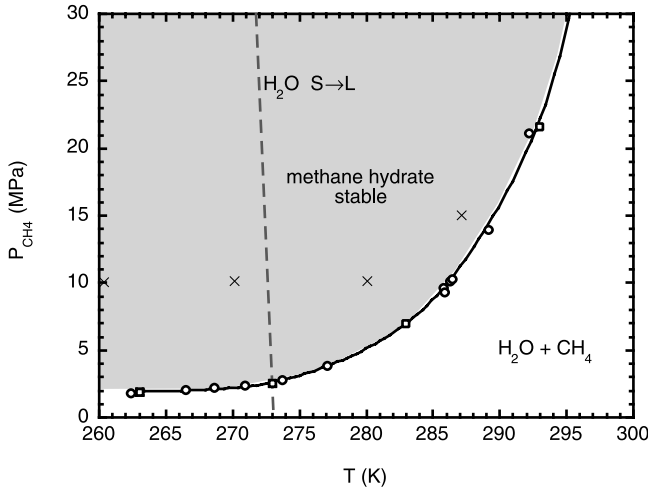


**Figure 4.** A portion of the phase diagram for methane plus water [Sloan, 1998]. The cross symbols show test conditions.

175 K, expeditiously close the vessel, and proceed with pressurization.

2. At  $T \approx 175$  K pressurize hydrostatically to 100 MPa in steps of roughly 5–10 MPa, measuring sample length at every step (from column displacement at the point where the internal force gage registers piston contact) and for the last three samples, recording the gas evolved from the sample at every step.  $P_{CH_4}$  was held at room pressure throughout this phase, which lasted anywhere from 1.5 to 5 h.

3. Still at  $T \approx 175$  K depressurize, remove the sample assembly, quench to 77 K, observe, measure, and photo-

graph, return the sample assembly to the vessel, and repressurize to roughly 50 MPa. This phase was skipped as unnecessary for the last two samples, after the first four showed that compaction was always uniform.

4. At  $P \approx 50$  MPa apply  $P_{CH_4} \approx 10$  MPa and warm the pressure vessel to 280 K, making occasional measurements of sample length. The edge of the methane hydrate stability field at 280 K is at  $P_{CH_4} = 5$  MPa (Figure 4). Once temperature has reached 280 K, increase  $P$  to 100 MPa to achieve final compaction. Measure sample length (again, with piston contact), which becomes the starting length for the purpose of calculating ductile strain. This entire procedure lasted from a few hours to nearly a day.

5. Conduct the deformation tests. These tests typically took a few days to 2 weeks to complete unless jacket failure ended the run prematurely.

6. Lower  $T$  to 175 K or below as quickly as possible holding  $P < 30$  MPa and  $P_{CH_4} \approx 10$  MPa Depressurize and move the sample assembly to storage at 77 K.

### 3. Results and Analysis

[11] Six samples of pure methane hydrate were tested. Experimental conditions and rheological results, including the ductile strain  $\epsilon$ , are listed in Table 1. The first two samples suffered jacket perforations early in the tests and so produced hydrostatic compaction data and only one strength measurement. These samples represented our first encounters with such warm temperatures at  $P = 100$  MPa step (4) in the procedure above. The indium encapsulation was sufficiently soft at 280 K that it intruded into the porous disc at the top of the sample at 100 MPa pressure, causing the jacket to perforate after several hours. We solved the

**Table 1.** Experimental Data

Run (step)	$P$ , MPa	$P_{CH_4}$ , MPa	$T$ , K	$\epsilon$	$\sigma$ , MPa	$\dot{\epsilon}$ s <sup>-1</sup>	Step begin	Step end
456	100	10	280					
457(1)	100	10	280.0	0.013	5.7 ± 0.2	1.34 × 10 <sup>-7</sup>		
458(1)	100	10	280.0	0.032	12.9 ± 0.1	6.11 × 10 <sup>-7</sup>		
458(2)	100	10	280.0	0.080	25.5 ± 0.5	3.20 × 10 <sup>-6</sup>	2.76 × 10 <sup>-6</sup>	3.62 × 10 <sup>-6</sup>
458(3)	100	10	280.0	0.135	44.6 ± 2.0	5.70 × 10 <sup>-5</sup>	2.54 × 10 <sup>-5</sup>	8.77 × 10 <sup>-5</sup>
458(4)	100	10	280.0	0.207	25.3 ± 0.4	7.24 × 10 <sup>-6</sup>		
458(5)	100	10	280.0	0.220	13.2 ± 0.1	7.20 × 10 <sup>-7</sup>	7.87 × 10 <sup>-7</sup>	6.52 × 10 <sup>-7</sup>
458(6)	100	10	280.0	0.246	26.7 ± 0.2	6.70 × 10 <sup>-6</sup>	4.32 × 10 <sup>-6</sup>	9.06 × 10 <sup>-6</sup>
458(7)	100	10	280.0	0.264	13.3 ± 0.1	1.16 × 10 <sup>-6</sup>		
459(1)	100	10	280.0	0.157	22.2 ± 0.3	5.90 × 10 <sup>-6</sup>	5.02 × 10 <sup>-6</sup>	6.82 × 10 <sup>-6</sup>
460(1)	100	10	259.5	0.012	17.8 ± 0.8	2.74 × 10 <sup>-8</sup>		
460(2)	100	10	259.5	0.032	34.3 ± 0.3	1.93 × 10 <sup>-7</sup>		
460(3)	100	10	259.5	0.070	51.7 ± 0.2	1.95 × 10 <sup>-6</sup>	1.42 × 10 <sup>-6</sup>	2.49 × 10 <sup>-6</sup>
460(4)	100	10	280.0	0.119	12.5 ± 0.1	2.07 × 10 <sup>-7</sup>		
460(5)	100	15	287.2	0.136	11.0 ± 0.4	7.34 × 10 <sup>-7</sup>		
460(6)	100	15	287.3	0.152	7.7 ± 0.3	1.86 × 10 <sup>-7</sup>		
460(7)	100	15	287.3	0.172	21.8 ± 0.3	4.09 × 10 <sup>-6</sup>		
460(8)	50	15	287.3	0.190	21.7 ± 0.2	9.29 × 10 <sup>-6</sup>		
461(1)	50	10	280.0	0.040	9.9 ± 0.1	1.64 × 10 <sup>-6</sup>		
461(2)	100	10	280.0	0.082	9.8 ± 0.2	6.08 × 10 <sup>-7</sup>		
461(3)	50	10	280.0	0.086	9.9 ± 0.2	8.51 × 10 <sup>-7</sup>		
461(4)	50	10	280.0	0.101	9.9 ± 0.1	8.73 × 10 <sup>-7</sup>		
461(5)	50	10	270.0	0.114	13.6 ± 0.4	3.23 × 10 <sup>-7</sup>		
461(6)	50	10	260.0	0.130	20.4 ± 0.3	1.86 × 10 <sup>-7</sup>		
461(7)	100	10	260.0	0.149	20.1 ± 0.2	1.22 × 10 <sup>-7</sup>		
461(8)	100	10	280.0	0.158	7.5 ± 0.3	2.82 × 10 <sup>-7</sup>		
461(9)	50	10	280.0	0.166	7.2 ± 0.1	2.97 × 10 <sup>-7</sup>		
461(10)	50	10	280.0	0.174	6.8 ± 0.2	3.61 × 10 <sup>-7</sup>		
461(11)	50	10	280.0	0.189	7.0 ± 0.2	5.77 × 10 <sup>-7</sup>		

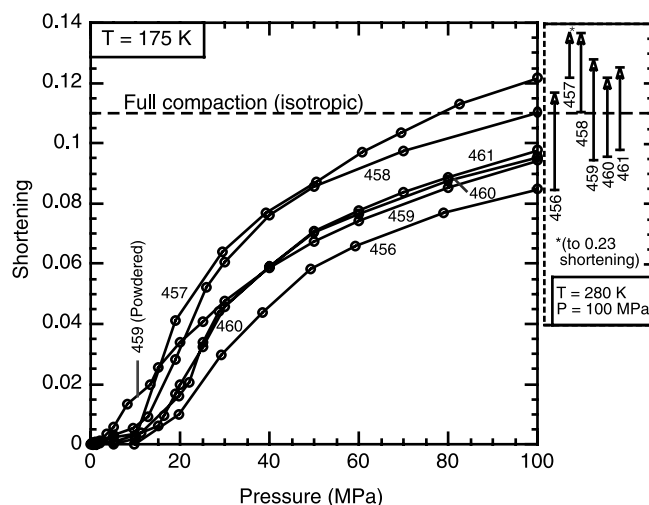


**Figure 5.** Hydrostatic compaction of all six samples. The curves give the shortening (length change normalized by starting length) as a function of pressure at 175 K. The inset at the right shows the additional shortening that results from warming to 280 K under a pressure of 100 MPa. Note that the solid material has initial cohesiveness but the powdered material does not.

problem by replacing the outer portion of the disc with an annulus of solid metal.

### 3.1. Hydrostatic Compaction

[12] Figure 5 shows the hydrostatic compaction curves during pressurization to 100 MPa for all six samples. Defining shortening as change in length divided by starting length, the samples generally shortened by a factor near 0.10 at 175 K, then shortened to an additional 0.03–0.04 when warmed to 280 K. Sample 257 was exceptional; it shortened by a factor of 0.12 at 175 K, and then to a total shortening of 0.23 at 280 K. Figure 3c shows that exceptionally high shortening occurred in the radial direction as well. The starting material has a bulk porosity of 29% if the material has fully reacted during synthesis [Stern *et al.*, 1998]. If the sample contracts isotropically, all linear dimensions will shorten by a factor of  $1 - (1 - 0.29)^{1/3} = 0.11$ . Variations in shortening during compaction probably mean slightly nonisotropic compaction rather than porosity variation, although the anomalous shortening of sample 457 (Figure 5) was matched by an anomalous diametral shortening, suggesting a starting porosity of over 50%. We have no explanation for the high porosity in this sample.

[13] The powdered sample, number 459, seems coincidentally to have had about the same starting porosity as the solid samples. However, note the difference in detail in the powdered sample versus the others at  $P < 20$  MPa in Figure 5. The powdered sample began compacting with the first application of pressure, whereas the solid samples had an initial cohesiveness that required  $P = 10$  MPa or more to overcome.

### 3.2. Gas Evolution During Compaction

[14] We routinely monitor gas evolution from samples during initial pressurization to assure jacket integrity before the start of every run. We noted qualitatively in early runs

that the volume of gas evolved from hydrate samples seemed higher than expected even when jackets were perfectly sealed. For the final three samples, we therefore measured gas evolution directly (Figure 6), by displacing water in a volumometer. Upon an increase in confining pressure, gas typically bubbled into the volumometer in a rapid burst, which then slowed and eventually stopped (indicating perfect jacket integrity). Each measurement in Figure 6 represents the cumulative volume of evolved gas once the bubbling stopped. The starting pore volume of the samples is about  $9 \text{ cm}^3$ , while the volume of gas evolved during compaction is consistently around  $70 \text{ cm}^3$  at STP. (By comparison, the full methane content of our  $\sim 30\text{-g}$  samples is about 6 L at STP.) Assuming the ideal gas law and taking the sample temperature as 175 K, the mass of gas evolved is approximately five times that which can be stored in the sample pore space at room pressure.

[15] The possibility that residual pressurized gas still resides in some of the macropores in the sample can be immediately eliminated by the fact that the powdered sample is one of the three in Figure 6. We have estimated the particle size of the powdered material to be near 0.1 mm. If the gas evolved during compaction originated in pores, those pores would have to be very small or a large fraction of them would be exposed at the surface of the fine grains. In fact, methane hydrate has recently been discovered to be microporous in certain circumstances [Kuhns *et al.*, 2000], but microporosity is not likely to be the explanation here: the basis for saying that our starting material has a porosity of  $29 \pm 1\%$  is a mass balance calculation (total mass of water and reacted methane are known precisely), plus confirmation of purity from X-ray diffraction, calorimetry, and dissociation tests in which the mass of evolved gas is

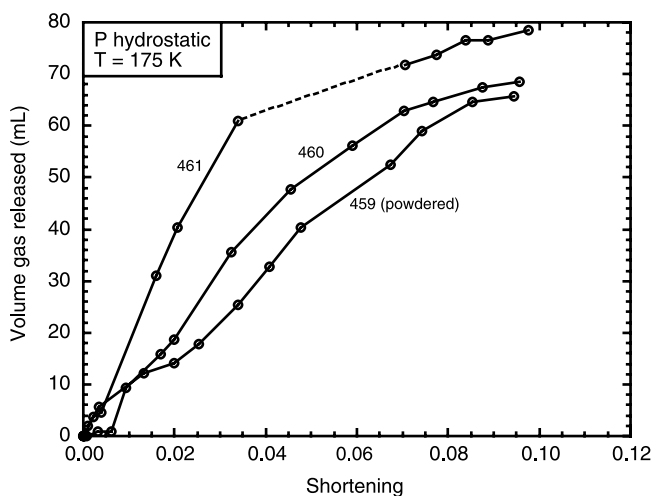


**Figure 6.** Gas evolution from three samples during hydrostatic compaction to 100 MPa (see also Figure 5). The interruption of the curve for sample 461 occurred at a moment of operator inattention when water backing up into the pore pressure line threatened to reach the sample itself. The line was cleared of water, reconnected, and the pressurization and monitoring of gas evolution continued, but an unknown amount of gas was not accounted for. The dashed line indicates that the absolute position of the final five data points with respect to the vertical axis is unknown.

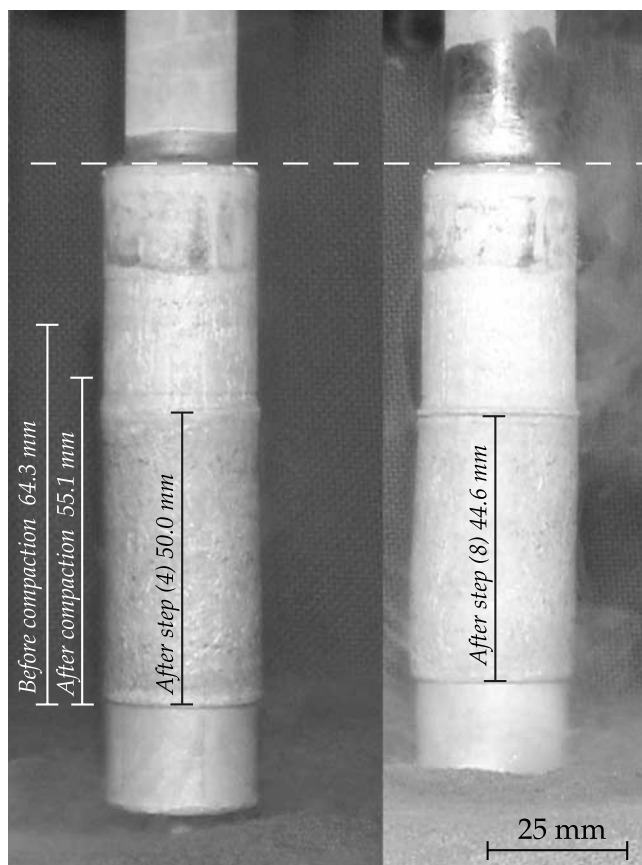


**Figure 7.** Sample 460 as it appeared at the end of deformation step (4) (left) and at the end of step (8) (right), illustrating the general uniformity of deformation throughout the compaction and ductile deformation phases of the experiment. The deformation, however, is not perfectly uniform: a subtle conical shape can be seen after step (4), where the diameter is approximately 1 mm larger at the bottom than the top, and is even more pronounced after step (8), where the difference has increased by an additional 0.25 mm.

measured to an accuracy better than 1 mol.% [Stern *et al.*, 1996, 1998, 2000]. Furthermore, SEM imaging of both starting material and fully compacted material shows that our hydrate is not meso- or microporous (Figure 2). If any microporosity remains in our samples, its total volume must be within the 1% error of the porosity determination, i.e.,  $\leq 0.1 \text{ cm}^3$ . To produce  $70 \text{ cm}^3$  of STP gas as observed, all micropores must therefore be filled with methane at approximately liquid density and all must become exposed during cold compaction, which seems highly unlikely.

[16] These observations suggest that we are observing a dynamic process of cage destruction (or breakdown) and reformation. One further indication that we are observing bound rather than free methane is that the gas evolution is partially reversible. The gas is released in steps that coincide with discrete (and often audible) steps in the densification. Following these discrete gas releases, water from the volumeter backs up into the tube, meaning that methane is being drawn back into the sample. (The evolved gas plotted in Figure 6 is the total of methane released; gas

molecules drawn back into the sample are not counted twice.) There are obviously complex processes at work here that require further investigation.

### 3.3. Creep Results

[17] The full set of rheological measurements is tabulated in Table 1. Test conditions were  $P = 50$  and  $100 \text{ MPa}$ ,  $4.5 \times 10^{-8} \leq \dot{\epsilon} \leq 10^{-4} \text{ s}^{-1}$ , and the four sets of  $(P_{\text{CH}_4}, T)$  shown in Figure 4. As explained above, the first two runs suffered jacket perforations following the compaction and warming, and yielded only one strength measurement. As anticipated,  $\dot{\epsilon}'$  reached a constant level in a few percent strain following a change in conditions, and experiments were multiple-step. One sample was deformed through 16% shortening at a single condition. Samples were shortened by about 20% and the distribution of strain in the samples, at least as judged from outside appearances was grossly uniform (Figure 7). A subtle but important deviation from uniformity is discussed below.

[18] Figure 8 shows all strength measurements from Table 1 except those from run 458, step (3), and beyond, which are shown separately in Figure 9b. For plotting purposes, all points in Figure 8 have been normalized to  $P = 50 \text{ MPa}$  using  $V^* = 19 \text{ cm}^3 \text{ mol}^{-1}$  (based on the data fits immediately below) in equation (1). Run-to-run scatter prevents a straightforward multivariate fit of the data to equation (1), as discussed below. Instead, we used individual pressure, temperature, and stress steps within a given run to constrain  $V^*$  and  $E^*$ , weighting each individual calculation by the inverse of the step size. We then normalized the data to a common pressure and temperature using these parameters and found  $A$  and  $n$  by a least squares fit to equation (1) reduced to the simple power law:

$$\dot{\epsilon} = A' \sigma^n.$$

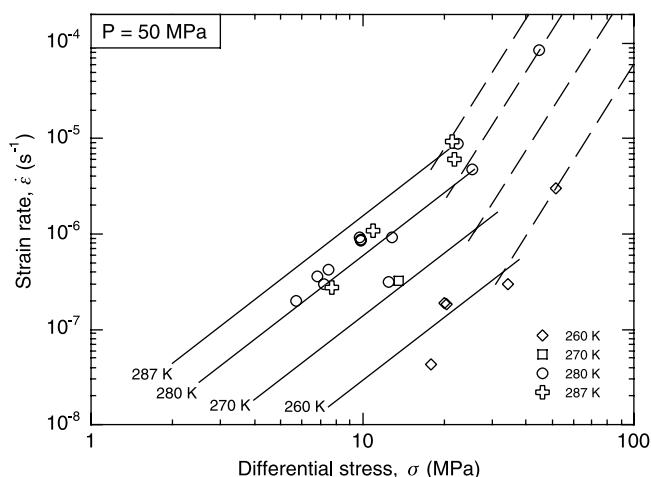


**Figure 8.** Rheological data from Table 1 plotted by temperature. Data for run 458 steps (3)–(7) are not included, but are shown in Figure 9b. Data are normalized to a common pressure of 50 MPa using  $V^* = 19 \text{ cm}^3 \text{ mol}^{-1}$  in equation (1). The solid lines are the fitted results to all but the two points at  $\sigma > 40 \text{ MPa}$ . The dashed lines, with slope  $n = 4.5$  are a possible fit to those two outliers. See text for further discussion.

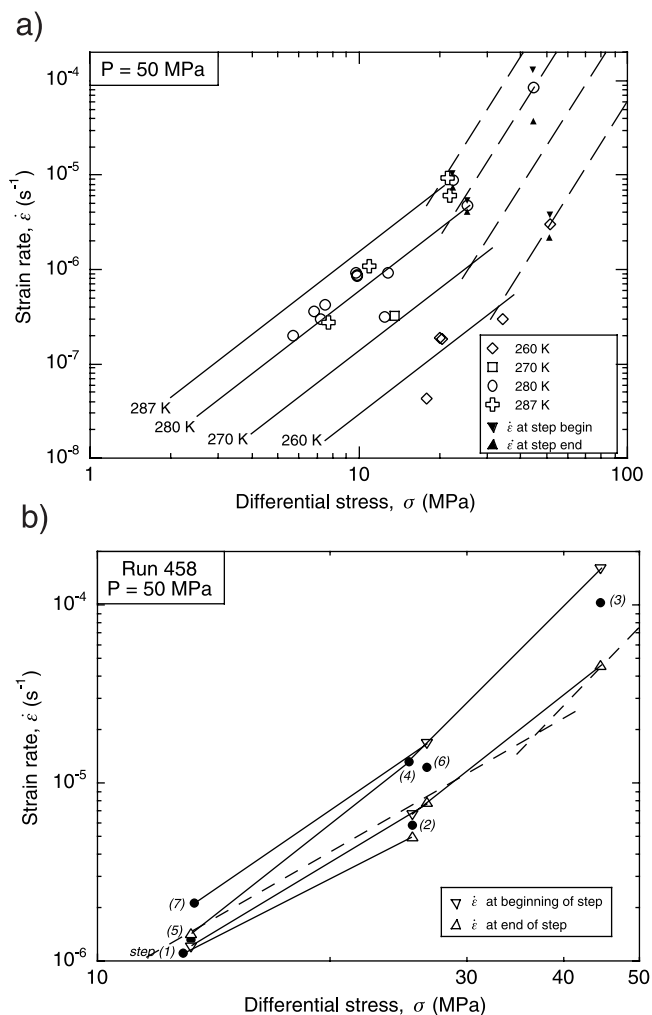


**Figure 9.** Strain softening, and in one case strain hardening, at high strain rates and stresses. (a) Beginning (upward pointing triangles) and ending (downward pointing triangles) strain rates in run steps where strain rate systematically changed by more than 10%, superimposed on the points in Figure 8; (b) detail of strain rate changes in run 458, with deformation step numbers labeled, and tie lines drawn from the end of one step to the beginning of the next. Dashed lines in Figure 9b are the high and low  $n$  flow laws at 280 K. All points corrected to 50 MPa as in Figure 8.

[19] The two measurements at highest stress, one at 260 K and the other at 280 K, were arbitrarily left out of the fit. Strain rates in both cases were significantly higher than expected on the basis of preceding measurements (Figure 8). Encountering a new deformation mechanism with higher-stress sensitivity, i.e., higher  $n$  in equation (1), at higher  $\sigma$  is common in geological and other materials. Rather than deflect the fit to include these two points, we treat them as outliers until the matter can be settled by further study.

[20] The results of the fit are as follows:  $V^* = 19 \pm 10 \text{ cm}^3 \text{ mol}^{-1}$  (4.5 pairs of measurements, from runs 460 and 461);  $E^* = 90,000 \pm 6000 \text{ J mol}^{-1}$  (9 pairs of measurements, from runs 460 and 461); and  $A = 10^{8.55} \text{ MPa}^{-n} \text{ s}^{-1}$ ,  $n = 2.2$ , with a correlation coefficient of 0.80. This fit is shown at the four

different run temperatures in Figure 8. *Chou et al.* [2000] discovered that a sI-sII phase transformation occurs in methane hydrate near  $P = 100 \text{ MPa}$  but we observe that the rheologies at  $P = 50$  and  $100 \text{ MPa}$  show the same dependence on  $T$  and  $\sigma$  (within experimental uncertainty), suggesting that this transformation did not occur in our samples or has no significant affect on rheology. There are too few data to constrain the higher-stress mechanism, but if we assume the same pressure and temperature dependence as the  $n = 2.2$  mechanism, then a value of  $n = 4.5$  matches the two measurements (dashed lines in Figure 8).

[21] Measurements over a wider temperature range would have allowed better resolution of  $E^*$  but were not achievable with the current apparatus design. Not anticipating the high strength of the sample material in question, we designed the force gage with a fairly thin wall (Figure 3d), giving it good stress resolution but a differential force limit roughly that of a 50-MPa stress on a 25-mm-diameter area. Staying below 50 MPa, it is evident from Figure 8 that making a reasonable number of measurements at  $T < 260$  would require prohibitively long run times to achieve significant strain. Simply constructing a thick-walled force gage to explore higher stresses may also not solve the problem because if the higher  $n$  deformation mechanism at  $\sigma > 50 \text{ MPa}$  (Figure 8) is real, it could easily have different temperature sensitivity than the  $n = 2.2$  mechanism.

### 3.4. Evolution of Water During Deformation

[22] There are two sets of observations that indirectly suggest that free water is generated during the ductile deformation of methane hydrate. The first is pronounced strain softening at high-strain rates, and the second is a greater swelling of sample diameter at the end away from the pore pressure line. There is excellent consistency across samples for these observations. Furthermore, we have directly observed dissociation during cold compaction, as discussed above. In no case have we detected free water in these samples by bulk X-ray diffraction, although that technique has a resolution limit of only about 2 vol.%. We performed a preliminary SEM examination of one deformed sample (sample 459) and also saw no obvious sign of free water (Figure 2c), although a small amount of ice could have been easily overlooked. The phase contrast between methane hydrate and ice is likely to be very faint, especially in fully dense material.

[23] At the highest stresses and strain rates, samples showed pronounced strain softening (increasing strain rate at fixed stress). Table 1 lists the strain rate at the beginning and at the end of numbered deformation steps where the difference between the two exceeded about 10%, and Figure 9a shows these high and low values with the mean from Figure 8. The strain softening was most pronounced in run 458, whose complete deformation history is shown in Figure 9b. This is also the only run where strain rate at a given stress was dependent on deformation history. For example, the strain rate at  $\sigma = 25 \text{ MPa}$  was twice as fast in step (4) as in step (2), which were separated by a step in which strain rate increased by a factor of well over 3. Significantly, no strain hardening occurred in step (4), and in the following step (5), significant strain hardening occurred (the only instance of this). Returning to  $\sigma = 25 \text{ MPa}$  in step (6), pronounced strain softening reappeared.

[24] More diametrical swelling occurred at the bottom than at the top of all deformed samples, giving them a conical shape. In two cases, the conical form was subtle: the final diameter of 459 was approximately 1.5 mm larger at the bottom than top. For 460, whose slight conical shape may be discernable in Figure 7, the difference between bottom and top diameters was about 1 mm after the fourth deformation step and 1.3 mm after the last step. On the other hand, the nonuniform swelling of 458 was so severe that the indium jacket ripped open at the bottom, one reason that we include only run steps (1) and (2) in the curve fit above. Nonuniform swelling in 461 was not as severe as in 458, but nevertheless, jacket perforation again occurred, probably near the end of the run, and the final step from that run was also excluded from the curve fit. Curiously, despite the obvious jacket perforations, no confining pressure was lost, even though in principle there was a leak path available through the pore pressure line. The sense of the conical shape of the samples, narrower at the end closer to the pore pressure line, argues against line blockage (by hydrate formation, for instance).

## 4. Discussion

### 4.1. Rheology

[25] Figure 10 shows that over the range of test temperatures and strain rates, methane hydrate is 20–30 times stronger than ice near the H<sub>2</sub>O melting temperature and that the contrast between hydrate and ice increases with decreasing temperature. This dramatic difference in strength is also suggested by other indirect observations in our lab: (1)  $P > 10$  MPa is required to initially compact as synthesized, 29% porous cylinders of methane hydrate (Figure 4), and (2) earlier comparative creep measurements of several composite ice plus methane hydrate samples showed far higher-strain rates and total strains in ice-rich sections than in hydrate-rich sections (Figure 1).

[26] This contrast in high-temperature ductile strength of ice and methane hydrate is at first glance surprising; ice itself is a relatively strong material at very high-homologous temperature  $T_h = T/T_{\text{melting}}$  [Goodman *et al.*, 1981], and has nearly the same density and oxygen-hydrogen bond angles and lengths as methane hydrate [Sloan, 1998]. Two key differences between these compounds, however, may give insight into their different mechanical behavior. Most crystalline metals and oxides (including ice) deform at  $T_h > 0.5$  by the coordinated motion of crystalline defects (point defects, dislocations, grain boundaries), often limited by rates of diffusion [Poirier, 1985]. The rate of molecular water diffusion may be as much as 2 orders of magnitude slower in gas hydrate than in ice [Sloan, 1998]. Second, the large hydrate sI unit cell (cubic, cell parameter 1.20 nm, 46 water molecules per unit cell) has about twice the linear dimension of that of ordinary ice  $I_h$  (hexagonal, cell parameters  $a = 0.45$  and  $c = 0.76$  nm, 4 water molecules per unit cell) [Sloan, 1998]. This size difference may make glide and climb motions of dislocations, as well as self-diffusion, more difficult, and thus increase the resistance of the material to intracrystalline plastic deformation.

[27] The high strength of sI methane hydrate has significant implications for the mechanical behavior of hydrate-bearing formations. Even in settings where hydrate concentration is

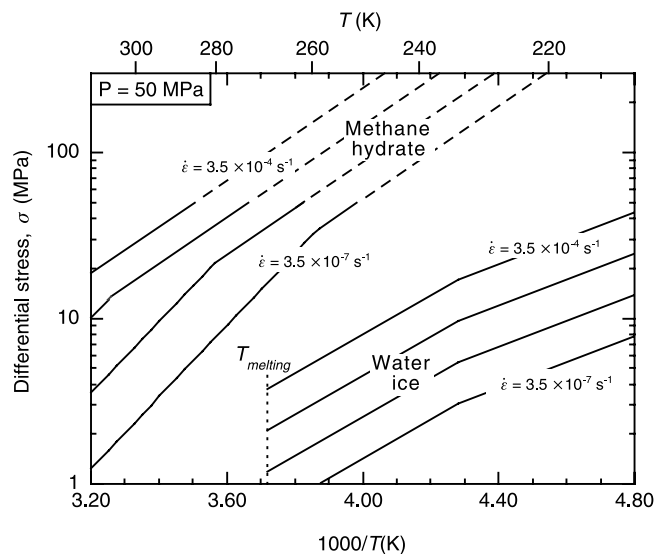


**Figure 10.** The strength of methane hydrate compared with that of water ice on an Arrhenius diagram of log stress versus inverse temperature. Lines give the locus of strengths at fixed strain rate for hydrate from this study and for ice from the study by Durham *et al.* [1997]. Strengths at four different strain rates, spaced 1 order of magnitude apart, are shown. The break in slope corresponds to a change in flow mechanism, i.e., a different set of flow constants in equation (1). For methane hydrate, the  $n = 4.5$  mechanism dominates (i.e., is weaker) over the  $n = 2.2$  mechanism at lower temperatures.

low, at high effective normal stresses (normal stresses minus pore pressure) frictional resistance and cohesion may be high enough so that time-dependent plastic deformation within the weakest grains of the aggregate may become important. By analogy with frozen soils, the markedly higher plastic flow strength of methane hydrate compared with that of water ice implies a much higher flow strength for hydrate aggregates compared with that of frozen soils. For example, large mass movements of hydrate-bearing sediments in the geologic record, likely triggered by pore pressure effects of gas hydrate decomposition [Kayen and Lee, 1991; Paull *et al.*, 1996], may have been amplified by the loss of high intrinsic strength associated with hydrate in the sediments.

[28] The effects of hydrate strength may extend beyond Earth. Carbon dioxide hydrate has been implicated in the development landforms on Mars [Kargel *et al.*, 2000]. Loveday *et al.* [2001] recently suggested that a 100-km-thick layer of sI methane hydrate exists near the surface of Titan. If true, the thermal structure of that moon would be profoundly different from those of ice/rock moons that do not contain the hydrate layer. The combined effects of high resistance to convective flow and unusually low thermal conductivity of the hydrate layer [Sloan, 1998] imply dramatically reduced heat transport from interior to surface and therefore higher internal temperatures for Titan. Hydrate stability at the base of the layer would in turn be affected and its 100-km thickness may be reduced.

[29] The strength difference between methane hydrate and ice begins to explain some of the past experimental

difficulties in dealing with hydrate deformation. The rheology of a polyphase aggregate depends on geometrical arrangement of phases and on the strength of those phases [Handy, 1994; Tullis *et al.*, 1991], but given the huge strength contrast, it is clear that even a small amount of free ice can seriously interfere with hydrate strength measurement. For example, it now appears that the first results of hydrate strength reported by Stern *et al.* [1996] were dominated by the  $\sim 25\%$  ice component. A mixture of 25% ice plus an undeformable phase is consistent with the measurements made by Stern *et al.* [1996].

[30] Finally, although ice is a demonstrably faulty analog for methane hydrate, one might also consider the role of grain boundary processes, such as grain boundary diffusion and grain boundary sliding, in these experiments. Deformation by these so-called grain-size-sensitive (GSS) processes can be activated in ice in the laboratory [Goldsby and Kohlstedt, 1997] more readily than in most other oxides. If the same behavior extends to hydrates, then the intergranular presence of small amounts of free water, which we have already speculated, has the potential to facilitate GSS deformation. Thus even the measurements in this study may have fallen short of representing the intrinsic strength of pure methane hydrate. GSS mechanisms are characterized by a strong dependence of strength on grain size, so again is testable by experiment if grain sizes can be controlled, and by a stress exponent of  $n = 2$  or less, not greatly different from what we observe here. Further investigation of GSS mechanisms in methane hydrate will help determine what the role of grain size is at these conditions, and whether, for example, the value of  $n = 2.2$  is transitional between GSS creep and higher  $n$  dislocation creep.

#### 4.2. Dissociation During Deformation

[31] The very high strength of methane hydrate with respect to water ice, the indirect evidence for evolution of water during deformation of hydrate, and the direct evidence for dissociation during cold compaction, all indicate that methane hydrate undergoes partial dissociation during deformation, even when the hydrate is deep within its own stability field. We suggest that the cold and warm processes are related in that some disruption of the lattice, whether microfracturing or the passage of lattice dislocations, causes material to decompose, and remain decomposed for sufficient time that other forces can segregate the free methane and water and limit their back reaction. In the case of cold compaction, it is the release of methane out the pore pressure line. In the case of warm creep, it is the nucleation and growth of pockets or films of liquid or solid water. The latter may help explain the higher strain rate sensitivity of creep at higher-strain rates (Figure 8). If the application of an axial load acts to make the weaker water phase migrate to free surfaces and if that migration rate is a function of axial load, then at higher rates of deformation (at the same load), water will accumulate more quickly in structurally important regions (such as between hydrate grains), causing the aggregate to become weaker. The reason that the samples swell more at the bottom than at the top is most likely due to better communication with the pore pressure line at the top. The removal of a very small amount of free water from the lattice is sufficient to keep the material at the top closer to pure hydrate, and therefore, stronger.

[32] If there is free water in the sample, and if that water is poorly drained, as the flare at the end of the sample away from the pore pressure line seems to indicate, then it is also likely that the effective confining pressure (the difference between the confining and pore pressure) in the lower section of the sample is low. Goetze's criterion [Kohlstedt *et al.*, 1995] that the effective pressure must exceed the differential stress to assure ductile deformation, may therefore not be met. One would then expect brittle behavior such as microcracking to appear and thus weaken the material. In either case, the water-assisted deformation or the appearance of brittle behavior, the measured strength will be less than the intrinsic strength of the material. Thus there is additional reason to suspect that the exceptional strengths measured in these tests may be only lower bounds on the strength of methane hydrate.

### 5. Conclusions

[33] Pure polycrystalline methane hydrate in high-temperature creep shows itself to be far stronger than anticipated on the basis of earlier work or on the basis of the strength of water ice. Where both are solid, the hydrate is 20 or more times stronger than water ice at the same conditions of temperature and strain rate. The direct influence of gas hydrate strength on gas hydrate-bearing formations increases approximately linearly with the proportion of hydrate in the formation. By analogy to frozen soils, local concentrations of hydrate in soils above 20–30% should show a noticeably higher strength than frozen water plus soil during geotechnical operations. Dispersed gas hydrates in marine sediments at typical volume concentrations of  $<5\%$ , on the other hand, probably will not have a direct rheological affect. Other properties of gas hydrates, such as cohesiveness with sediment particles, and more importantly the overall phase stability, probably have greater influence on key formation properties such as slope stability. At the other extreme, the presence of a planet-wide, 100-km-thick layer of very strong, thermally insulating methane hydrate must have a first-order effect on the evolution of Titan.

[34] Fundamental processes during gas hydrate deformation may still need to be identified. Inelastically deforming methane hydrate apparently causes it to dissociate, even at pressures and temperatures well within its phase stability field. The effect of strain and other variables on dissociation has yet to be quantified, but the mechanical effects of the release of small amounts of liquid or solid water, given the distinct strength contrast between ice and methane hydrate, can be easily measured.

[35] This investigation of creep of methane hydrate is a necessary first step toward understanding the inelastic response of hydrate-bearing formations in complex settings. Controlled experiments on synthetic hydrate-sediment aggregates are clearly called for in order to determine what roles gas hydrate rheology may play in governing the inelastic behavior of natural sediment-hydrate aggregates.

[36] **Acknowledgments.** The work was performed under the auspices of the U.S. Department of Energy by the Lawrence Livermore National Laboratory under contract W-7405-ENG-48. This work was supported in part by NASA under work order W-19,075 and by the Natural Gas Hydrate Program of U.S. Department of Energy, National Energy and Technology Laboratory.

## References

- Andersland, O. B., and B. Ladanyi, *Frozen Ground Engineering*, 352 pp., Chapman and Hall, New York, 1994.
- Cameron, I., Y. Handa, and T. H. W. Baker, Compressive strength and creep behavior of hydrate-consolidated sand, *Can. Geotech. J.*, *27*, 255–258, 1990.
- Chou, I.-M., A. Sharma, R. C. Burruss, J. Shu, H.-K. Mao, R. J. Hemley, A. F. Goncharov, L. A. Stern, and S. H. Kirby, Transformations in methane hydrates, *Proc. Natl. Acad. Sci. U. S. A.*, *97*, 13,484–13,487, 2000.
- Collett, T. S., Natural gas hydrate as a potential energy resource, in *Natural Gas Hydrate in Oceanic and Permafrost Environments*, edited by M. D. Max, pp. 123–136, Kluwer Acad., Norwell, Mass., 2000.
- Dallimore, S. R., and T. S. Collett, Regional gas hydrate occurrences, permafrost conditions, and Cenozoic geology, Mackenzie Delta area, in *Scientific Results from JAPEX/JNOC/GSC Mallik 2L-38 Gas Hydrate Research Well, Mackenzie Delta, Northwest Territories, Canada*, edited by T. S. Collett, pp. 31–43, Geol. Surv. of Canada, Ont., 1999.
- Durham, W. B., S. H. Kirby, and L. A. Stern, Creep of water ices at planetary conditions: A compilation, *J. Geophys. Res.*, *102*, 16,293–16,302, 1997.
- Goldspy, D. L., and D. L. Kohlstedt, Grain boundary sliding in fine-grained ice I, *Scr. Mater.*, *37*, 1399–1406, 1997.
- Goodman, D. J., H. J. Frost, and M. F. Ashby, The plasticity of polycrystalline ice, *Philos. Mag. A*, *43*, 665–695, 1981.
- Guerin, G., D. Goldberg, and A. Meltse, Characterization of in situ elastic properties of gas hydrate-bearing sediments on the Blake Ridge, *J. Geophys. Res.*, *104*, 17,781–17,795, 1999.
- Handy, M. R., Flow laws for rocks containing two non-linear viscous phases: A phenomenological approach, *J. Struct. Geol.*, *16*, 287–301, 1994.
- Helgerud, M. B., Wave speeds in gas hydrate and sediments containing gas hydrate: A laboratory and modeling study, Ph.D. thesis, Stanford Univ. Press, Stanford, Calif., 2001.
- Holbrook, W. S., H. Hoskins, W. T. Wood, R. A. Stephen, and D. Lizarralde, Methane hydrate and free gas on the Blake Ridge from vertical seismic profiling, *Science*, *273*, 1840–1843, 1996.
- Jakosky, B. M., B. G. Henderson, and M. T. Mellon, Chaotic obliquity and the nature of the Martian climate, *J. Geophys. Res.*, *100*, 1579–1584, 1995.
- Kargel, J. S., K. L. Tanaka, V. R. Baker, G. Komatsu, and D. R. MacAyeal, Formation and dissociation of clathrate hydrates on Mars: Polar caps, northern plains, and highlands, *Lunar Planet. Sci. XXXI*, 1891, 2000.
- Kayen, R. E., and H. J. Lee, Pleistocene slope instability of gas hydrate-laden sediment on the Beaufort Sea margin, *Mar. Geotech.*, *10*, 125–141, 1991.
- Kohlstedt, D. L., B. Evans, and S. J. Mackwell, Strength of the lithosphere: Constraints imposed by laboratory measurements, *J. Geophys. Res.*, *100*, 17,587–17,602, 1995.
- Kuhs, W. F., A. Kalproth, F. Gotthardt, K. Techmer, and T. Heinrichs, The formation of meso- and macroporous gas hydrates, *Geophys. Res. Lett.*, *27*, 2929–2932, 2000.
- Kvenvolden, K. A., Gas hydrates—geological perspective and global change, *Rev. Geophys.*, *31*, 173–187, 1993.
- Kvenvolden, K. A., Natural gas hydrate: Introduction and history of discovery, in *Natural Gas Hydrate in Oceanic and Permafrost Environments*, edited by M. D. Max, pp. 9–16, Kluwer Acad., Norwell, Mass., 2000.
- Loveday, J. S., R. J. Nelmes, M. Guthrie, S. A. Belmonte, D. R. Allan, D. D. Klug, J. S. Tse, and Y. P. Handa, Stable methane hydrate above 2 GPa and the source of Titan's atmospheric methane, *Nature*, *410*, 661–663, 2001.
- Lunine, J. I., and D. J. Stevenson, Thermodynamics of clathrate hydrate and low and high pressures with application to the outer solar system, *Astrophys. J. Suppl. Ser.*, *58*, 493–531, 1985.
- Martinson, O., Mass movements, in *Geological Deformation of Sediments*, edited by A. Maltman, pp. 127–165, Chapman and Hall, New York, 1994.
- Miller, S. L., and W. D. Smythe, Carbon dioxide hydrate and floods on Mars, *Science*, *170*, 531–533, 1970.
- Mulder, T., and J. Alexander, The physical character of subaqueous sedimentary density flows and their deposits, *Sedimentology*, *48*, 269–299, 2000.
- Parameswaran, V. R., M. Pardis, and Y. P. Handa, Strength of frozen sand containing tetrahydrofuran hydrate, *Can. Geotech. J.*, *26*, 479–483, 1989.
- Paull, C. K., W. J. Buelow, W. Ussler III, and W. S. Boroski, Increased continental-margin slumping frequency during sea-level lowstands above gas hydrate-bearing sediments, *Geology*, *24*, 143–146, 1996.
- Poirier, J.-P., *Creep of Crystals*, 260 pp., Cambridge Univ. Press, New York, 1985.
- Sloan, E. D., *Clathrate Hydrates of Natural Gases*, 2nd ed., 705 pp., Marcel Dekker, New York, 1998.
- Stern, L. A., S. H. Kirby, and W. B. Durham, Peculiarities of methane clathrate hydrate formation and solid-state deformation, and the associated superheating of water ice, *Science*, *273*, 1843–1848, 1996.
- Stern, L. A., S. H. Kirby, and W. B. Durham, Polycrystalline methane hydrate: Synthesis from superheated ice, and low-temperature mechanical properties, *Energy Fuels*, *12*, 201–211, 1998.
- Stern, L. A., S. H. Kirby, W. B. Durham, S. Circone, and W. F. Waite, Laboratory synthesis of pure methane hydrate suitable for measurement of physical properties and decomposition behavior, in *Natural Gas Hydrate in Oceanic and Permafrost Environments*, edited by M. D. Max, pp. 323–348, Kluwer Acad., Norwell, Mass., 2000.
- Tullis, T. E., F. G. Horowitz, and J. Tullis, Flow laws of polyphase aggregates from end-member flow laws, *J. Geophys. Res.*, *96*, 8081–8096, 1991.
- Winters, W. J., W. F. Waite, W. P. Dillon, D. H. Mason, and I. A. Pecher, Relationships between frozen and gas hydrate-containing sediment, in 2nd Russian Conference on Geocryology, Russia, 2001.
- Zhang, W., W. B. Durham, L. A. Stern, and S. H. Kirby, Experimental deformation of methane hydrate: New results, *Eos Trans. AGU*, *80(17)*, Spring Meet. Suppl., S337, 1999.

W. B. Durham, Lawrence Livermore National Laboratory, L-201, University of California, P.O. Box 808, Livermore, CA 94550, USA. (durham1@llnl.gov)

S. H. Kirby and L. A. Stern, U.S. Geological Survey, Menlo Park, CA 94025, USA.

W. Zhang, West Virginia University, Morgantown, WV 26506, USA.